



Analytical analysis of working face passive stability during shield tunneling in frictional soils

Wei Liu¹ · Peixin Shi¹ · Lijuan Chen¹ · Qiang Tang¹

Received: 21 May 2018 / Accepted: 2 November 2018 / Published online: 14 November 2018
© Springer-Verlag GmbH Germany, part of Springer Nature 2018

Abstract

This paper develops the 2D and 3D kinematically admissible mechanisms for analyzing the passive face stability during shield tunneling using upper-bound analysis. The mechanisms consider trapezoidal distribution of support pressure along tunnel face and partial failure originated at tunnel face above invert. For cohesionless soils, the support pressure is a function of soil effective frictional angle φ' which determines the inclination of failure block and the normalized soil cover depth C/D (soil cover depth/tunnel diameter) which affects the origination of the passive failure. For cohesive soils, the support pressure is a function of φ' , C/D , and the effective cohesion c' . The cohesion c' has a relatively smaller impact on the support pressure than φ' and C/D have. The mechanisms are verified by comparing the current solutions with a previous upper-bound solution. The comparison shows that the current solutions are a general solution which is capable of predicting the passive face failure originated at any depth along tunnel face and the previous solution is a particular solution with the assumption that the face failure originated at tunnel invert. The mechanisms are validated through application to a practical project of shallowly buried, large diameter underwater tunnel. The validation shows that the mechanisms are capable of assessing the tunnel face passive instability rationally.

Keywords Partial failure · Shield tunnel · Support pressure · Upper-bound analysis · Working face instability

1 Introduction

Recent decades have seen an increasing pace of urban tunnel construction driven by the demand of underground space utilization and the advancement of tunneling technique. For example, in China, approximately 2500 km of subway tunnels was constructed in the past two decades and additional 5000 km of subway tunnels was planned for the next two decades [24]. Most of the soft ground urban tunnels were mechanized tunnels driven by earth pressure

balanced (EPB) shield or slurry shield (SS). Compared with EPB shield tunneling, the SS tunneling controls ground movement better in loosely saturated soils and is used more widely in densely populated urban areas underlain with unstable subsurface strata [11, 17].

During SS tunneling, the stability of excavation face is protected by maintaining the slurry pressure in the front cabin to support the external earth pressure. Inadequate or excessive slurry pressure may cause active or passive ground failures which generate large ground deformation consequently. The active ground failure may cause the collapse of the excavation face and has been investigated intensively [1, 2, 4, 6, 8, 12–14, 16, 18, 20, 21, 28]. The passive ground failure may cause blowout of the ground. Field observation shows that the passive failure is potentially more likely to occur during the excavation of shallowly buried tunnels [3, 7, 32]. The field observation is also supported by laboratory model tests [22, 29]. Typical tunnel design requires 1–1.5 times of tunnel diameter of soil cover above the crown to reduce the risk of passive failure [30]. For large diameter tunnels, this criterion is

✉ Peixin Shi
pxshi@suda.edu.cn

Wei Liu
ggoulmmeng@suda.edu.cn

Lijuan Chen
chenlj@suda.edu.cn

Qiang Tang
tangqiang@suda.edu.cn

¹ School of Urban Rail Transportation, Soochow University, 8 Jixue Rd., Suzhou 215131, China

difficult to meet under certain conditions, for example, when crossing rivers. Recently, there have been several large diameter tunnels crossing rivers in China, for example, the 15.4-m-diameter tunnel crossing the Yangtze River with 11.69 m of soil cover in Shanghai and the 11.6-m-diameter Huanbei tunnel crossing the Dong River with 2.5 m of soil cover in Hangzhou. For these tunnels, the passive failure creates a major risk during tunneling and requires care examination during design.

The stability of tunnel face is typically analyzed using limit analyses which include lower-bound and upper-bound analyses. The lower-bound analysis determines the external loads of the system based on the stress distribution that satisfies the equilibrium equation, boundary conditions and material yield criterion. The upper-bound analysis determines the external loads on a kinematically admissible mechanism by balancing the rate of work done by external forces with the rate of work which can be dissipated internal the system. The velocity field applied in the upper-bound analysis is convenient and is contained in actual collapse mode or mechanism [5]. Therefore, the upper-bound analysis is popularly used for face stability analysis.

During SS tunneling, the soil and hydrostatic pressures are balanced by the slurry pressure which is adjusted by controlling the inflow and outflow of the slurry in the cabin. The slurry pressure follows a trapezoidal distribution with a linear increase with depth at a rate of the unit weight of the slurry, typically ranging between 10 and 12 kN/m³ [11, 15]. For small diameter tunnels, the slurry pressure can be approximated as a uniform distribution with the resultant force acting on the center of the working face [1]. Based on this assumption, Davis et al. [8] proposed a 2D block failure model to investigate the face stability using upper-bound analysis. Leca and Dormieux [14] introduced a 3D conical model into the upper-bound analysis to evaluate the support pressure against passive failure. Their model was improved into a multi-block model along the sliding surface to investigate the passive failure by Oberlé [23] and Soubra [25, 26]. Mollon et al. [20, 21] proposed a rational model using spatial discrete technique to investigate the full-face failure of circular tunnels. Zhang et al. [31] recently investigated the face collapse and blowout failure of circular tunnels with the extension of the three-dimensional mechanism of a continuous velocity field with a toric envelope for slope stability [10, 19].

For large diameter tunnels, the difference between the slurry pressure at the crown and invert of the tunnel face becomes large and the error associated with the assumption of a uniform slurry pressure distribution becomes high. At the same time, the earth pressure on the tunnel face also follows a trapezoidal distribution. The earth pressure consists of hydrostatic pressure, which linearly increases with depth at a slope of 9.8 kN/m³, and the soil pressure, which

linearly increases with depth and ranges between active and passive earth pressures, dependent on the speed of machine penetration. As the tunnel diameter increases, the difference of the earth pressure between the crown and invert increases, making the control of the slurry pressure difficult. Due to the insufficient support pressure, some patterns of partial face collapse which are restricted to a zone around the upper part of the tunnel face were illustrated by Anagnostou and Kovári [1]. On the other hand, Dias et al. [9] found that during large diameter SS tunneling, the excessive support pressure caused a so-called partial passive failure based on numerical simulations. At the working face, the partial passive failure originates from the lower part instead of the invert of tunnel face and extends to the ground surface. Li et al. [15] analyzed the partial passive failure during large diameter SS tunneling in clay and found that the partial passive failure may take place before the full-face failure under excessive support pressure. This research indicates that the upper part of the face is vulnerable to passive failure as the support pressure is significantly higher than the earth pressure.

This paper develops the 2D and 3D kinematically admissible mechanisms for analyzing the partial passive instability during SS tunneling using upper-bound analysis. After Introduction, the 2D and 3D kinematically admissible mechanisms are derived in Sect. 2. The effects of soil parameters and tunnel burial depth on the support pressure are explored, and the support pressure from the current solutions is compared with that from the previous upper-bound solution in Sect. 3. The mechanisms are applied to a practical project of shallowly buried large diameter underwater tunnel in Hangzhou, China, in Sect. 4, followed by the conclusions presented in Sect. 5.

2 Upper-bound solution for passive face stability

2.1 Support pressure

Figure 1 shows the distribution of support pressure during SS tunneling in a homogenous soil stratum. The diameter of the shield is D . The soil cover depth above tunnel crown is C which is normalized with the tunnel diameter D to define a dimensionless parameter C/D . The surcharge on the ground surface is σ_s . The groundwater table is assumed at the ground surface. The water depth at tunnel crown is H . The unit weight of water is γ_w , and the effective unit weight of the soil is γ' . The slurry pressure follows a trapezoidal distribution with a linear increase with depth at a rate of slurry weight γ_F . The origination of the passive failure is characterized by a normalized depth $\eta = D_L/D$

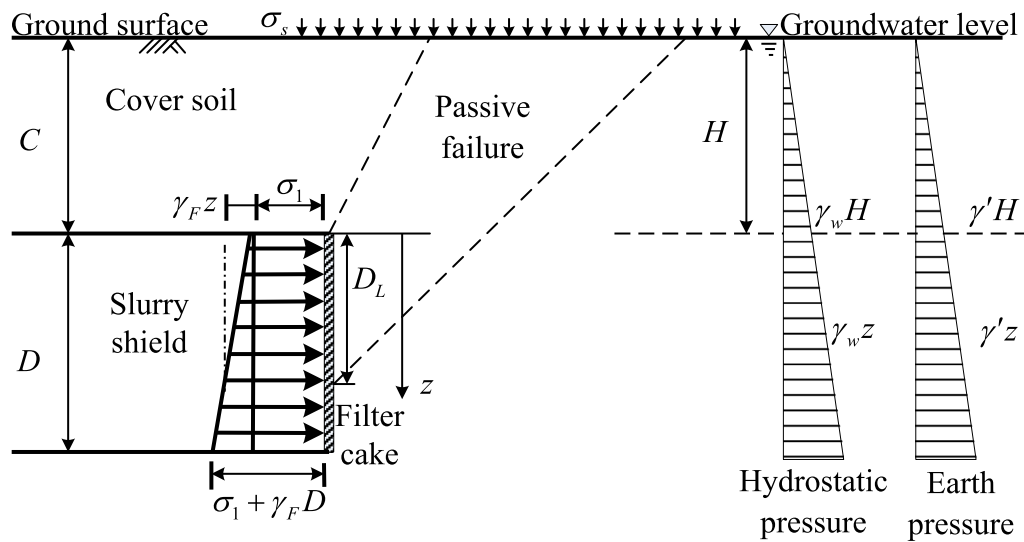


Fig. 1 Distribution of earth pressure and slurry pressure

where D_L is the height of failure origination measured from tunnel crown.

The trapezoidal support pressure σ_t is divided to two parts: the rectangular part σ_1 and the triangular part. At depth z , the total support pressure is

$$\sigma_t = \sigma_1 + \gamma_F z. \tag{1}$$

The effective support pressure σ'_t is

$$\sigma'_t = \sigma_1 + (\gamma_F - \gamma_w)z - \gamma_w H. \tag{2}$$

2.2 Upper-bound analysis

The ultimate support pressure at tunnel face during passive failure was evaluated through upper-bound analysis which estimates the support load by considering a kinematically admissible failure mechanism for which the work rate P_e of the external loads applied to the system is equaled to the work rate P_v dissipated within the system ($P_e = P_v$) [5, 14]. Two mechanisms MI for two-dimensional (2D) and MII for three-dimensional (3D) analyses were performed. The soil mechanical behavior is modeled by means of a rigid–perfectly plastic constitutive relationship with a failure condition defined according to the Mohr–Coulomb criterion and an associated flow rule. The shear strength of the soil is characterized by the effective cohesion c' and frictional angle ϕ' . In both mechanisms, along any failure surface \sum_d , the angle θ_d between the discontinuity velocity and \sum_d satisfies $\phi' \leq \theta_d \leq \pi - \phi'$ [14].

Mechanism MI assumes a planar rigid block sliding under the plain-strain condition. The dimension perpendicular to the plane is taken as unity. As shown in Fig. 2, the failure is triggered by the sliding of the rigid tetragonal

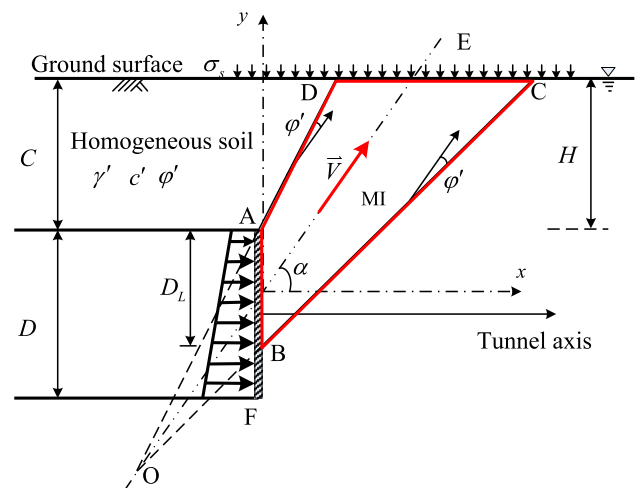


Fig. 2 Mechanism MI

block ABCD. The length of AB is D_L . Segment DC represents the length of the failure block at ground surface. Lines BC and AD are the sliding surfaces intersecting at point O, and the angle AOB is $2\phi'$. Line OE is the internal bisector of angle AOB. The velocity \vec{V} of the movement of the tetragonal block ABCD is parallel to axis OE which has an inclination angle of α with respect to the horizontal direction. The α value determines the inclination angle of the failure block. The higher the α value is, the steeper of the failure block is. The origination of the face failure is defined by the depth ratio $\eta = D_L/D$. The higher the value of η is, the deeper the failure face originates, and the larger the failure block is.

The work rate of the external loads on block ABCD consists of three components: from the pressure σ'_t on AB, from the surcharge σ_s on DC and from the effective weight

of soil within the block ABCD. The work dissipates during the translational movement of the rigid block ABCD along AD and BC. With $P_e = P_v$, the support pressure can be derived. The detailed derivation is presented in “Appendix 1”. The 2D solution of the support pressure is

$$\sigma_1^{2D} = \gamma' D N_\gamma^{2D} + \sigma_s N_s^{2D} + c' N_c^{2D} - (\gamma_F - \gamma_w) \eta D / 2 + \gamma_w H \tag{3}$$

where

$$N_\gamma^{2D} = \frac{\tan \alpha}{2\eta} \left[\frac{(C/D + \eta)^2}{\tan(\alpha - \phi')} - \frac{(C/D)^2}{\tan(\alpha + \phi')} \right] \tag{4}$$

$$N_s^{2D} = \frac{\tan \alpha}{\eta} \left[\frac{C/D + \eta}{\tan(\alpha - \phi')} - \frac{C/D}{\tan(\alpha + \phi')} \right] \tag{5}$$

$$N_c^{2D} = \cot \phi' (N_s^{2D} - 1). \tag{6}$$

Given c' , ϕ' and C/D , the coefficients N_γ^{2D} , N_s^{2D} and N_c^{2D} are a function of α and η . The support pressure can be calculated by searching the optimal value of α and η leading to a minimum support pressure. The calculation is performed by the commercial software Mathematica 5.0.

The mechanism MIII assumes a truncated conical block failure mechanism in light of the Leca and Dormieux’s model [14]. The failure mechanism is shown in Fig. 3. The failure block B is defined by the cone C truncated by the cone C' . The two cones C and C' have the same an apex at point Ω and opening angle $2\phi'$. The base of the cone C is at ground surface defined by the ellipse Σ with the semi-axis a and b . The base of the cone C' is at tunnel surface defined by the ellipse Σ' with the semi-axis a' and b' . The velocity

\bar{V} of the moving block B is parallel to the axis of cones C and C' . The height of the failure block at the face is D_L equal to the long semi-axis a' . It is also characterized by $\eta = D_L/D$.

The external loads applied on the moving block B include the support pressure on Σ' , the surcharge on Σ , and the effective soil weight of the block B . The dissipation occurs along the discontinuity surface of the rigid block. With $P_e = P_v$, the support pressure is calculated. The detailed derivation is presented in “Appendix 2”. The 3D upper-bound solution of the support pressure is

$$\sigma_1^{3D} = \gamma' D N_\gamma^{3D} + \sigma_s N_s^{3D} + c' N_c^{3D} - (\gamma_F - \gamma_w) \eta D / 2 + \gamma_w H. \tag{7}$$

where

$$N_\gamma^{3D} = \frac{\tan \alpha}{3\eta^2} (R_A R_B - \eta^2 R_C), \tag{8}$$

$$N_s^{3D} = \frac{\tan \alpha R_A}{\eta^2}, \tag{9}$$

$$N_c^{3D} = \cot \phi' (N_s^{3D} - 1). \tag{10}$$

The coefficients R_A , R_B and R_C in Eqs. (8), (9) and (10) are

$$R_A = \sqrt{\tan(\alpha - \phi') \tan(\alpha + \phi')} \left[\frac{\eta + C/D}{\tan(\alpha - \phi')} - \frac{C/D}{\tan(\alpha + \phi')} \right]^2, \tag{11}$$

$$R_B = \frac{\eta}{2} \left(1 + \frac{\sin 2\alpha}{\sin 2\phi'} \right) + \frac{C}{D}, \tag{12}$$

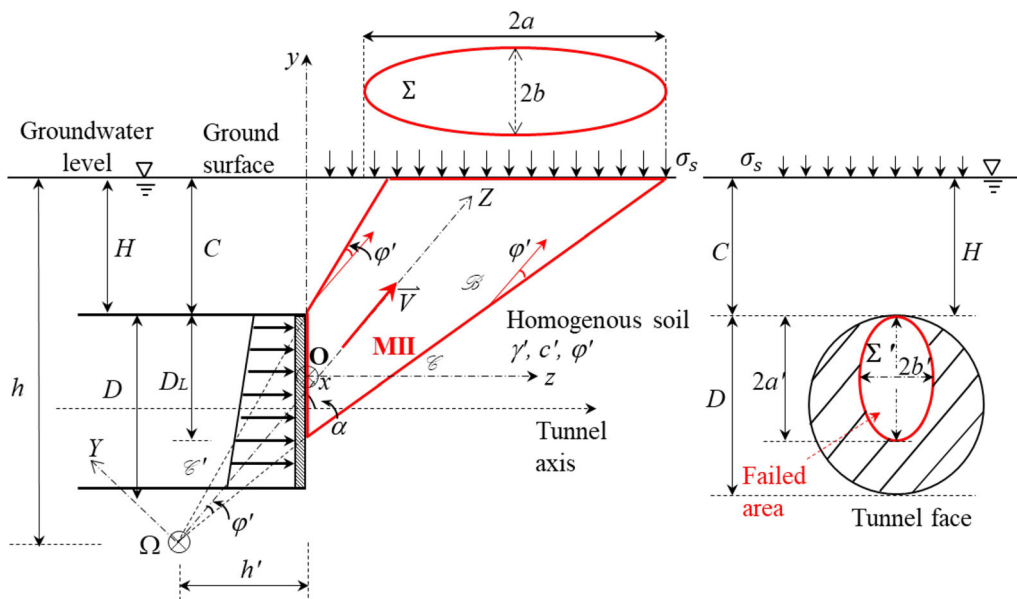


Fig. 3 Mechanism MIII

$$R_C = \frac{\eta \cos(\alpha - \phi') \cos(\alpha + \phi')}{\sin 2\phi'} \tag{13}$$

Similar to the 2D solution, given c' , ϕ' and C/D , the parameters N_γ^{3D} , N_s^{3D} and N_c^{3D} are a function of α and η . The support pressure is obtained by searching the optimal value of α and η resulting in a minimum support pressure. The calculation is performed by Mathematica 5.0.

3 Support pressure analysis

3.1 Discussion on the coefficients

The support pressure σ_1 is a function of two variables α and η which determine the inclination and origination of the failure zone, respectively. To analyze the variation of the parameters α and η , the example, as shown in Fig. 1, was analyzed with three different C/D ratios 0.25, 0.5 and 0.75. The effective unit weight of the soil was assumed as $\gamma' = 9.8 \text{ kN/m}^3$. The surcharge was taken as zero ($\sigma_s = 0 \text{ kPa}$). Since the unit weight γ_F of the slurry is close to that of water, it is assumed $\gamma_F = \gamma_w$ to simplify the calculation, such that the item $(\gamma_F - \gamma_w)\eta D/2 = 0$ in Eqs. (4) and (8). The analyses show that the term $(\gamma_F - \gamma_w)\eta D/2$ accounts for a very portion of the support pressure even with high γ_F value.

The analyses started with cohesionless soil (i.e., $c' = 0$), for which Eqs. (4) and (8) are simplified as $\sigma_1^{2D} = \gamma' DN_\gamma^{2D} + \gamma_w H$ and $\sigma_1^{3D} = \gamma' DN_\gamma^{3D} + \gamma_w H$, respectively. For a constant $\gamma_w H$, σ_1 is solely depended on N_γ . Table 1 lists the α , η and N_γ values for each case. This table shows that the parameter α is a function of ϕ' and is virtually independent on C/D . This means the inclination angle of the failure block is solely determined by the soil frictional angle but is not related to tunnel burial depth ratio. With the same ϕ' , α^{2D} is a slightly higher than α^{3D} . As ϕ' varies from 10° to 30° , α^{2D} varies from 48.7° to 58.6° while α^{3D}

varies from 47.0° to 49.4° . The α^{3D} value is approaching the optimal $\alpha \approx 49^\circ$ as calculated by Leca and Dormieux [14] who assumed the failure originated from the tunnel invert.

The parameter η is a function of both ϕ' and C/D . In general, the η value increases with the increase in ϕ' and C/D . The increase in the η value means the origination of the failure block moving toward the tunnel invert. The increase rate of η is higher in the 3D solution than the 2D solution. When $C/D = 0.25$, as ϕ' increases from 10° to 30° , η^{2D} increases from 0.18 to 0.25 and η^{3D} increases from 0.31 to 0.47. Both η^{2D} and η^{3D} are smaller than 0.5, indicating that the failure originates from the upper part of the tunnel face. When $C/D = 0.5$, η^{2D} increases from 0.36 to 0.50 while η^{3D} increases from 0.62 to 0.94, indicating that the failure zone originates from the upper part of the tunnel face in the 2D solution and from the lower part of the tunnel face in the 3D solution. Particularly, $\eta^{3D} = 0.94$ indicates that the failure zone originates from a depth near the invert of the tunnel. When $C/D = 0.75$, the 2D solution predicts the failure originates from the lower part of the tunnel face and the 3D solution predicts the failure originates near or at the tunnel invert.

Figures 4 and 5 show the failure pattern of mechanisms MI and MII as a function of ϕ' and C/D . Figure 4a shows the variation of failure block when C/D varies from 0.25 to 0.75, while ϕ' keeps at a constant of 20° . With the increase in the C/D value, the inclination angle α^{2D} of the failure block keeps constant, while the depth ratio η^{2D} linearly increases, indicating that the failure block originates toward down the tunnel invert. At the same time, the area of the failure block increases and the failure zone expands at the ground surface. The area of the failure block increases by 879% from 16.5 to 145 m² and length of failure block at ground surface triples when the C/D increases from 0.25 to 0.75. Figure 4b shows the variation of failure block when ϕ' varies from 10° to 30° , while C/D

Table 1 Optimal value of α , η and N_γ

	$C/D = 0.25$			$C/D = 0.5$			$C/D = 0.75$		
	α^{2D}	η^{2D}	N_γ^{2D}	α^{2D}	η^{2D}	N_γ^{2D}	α^{2D}	η^{2D}	N_γ^{2D}
$\phi' = 10^\circ$	48.7	0.18	0.61	48.5	0.36	1.22	48.7	0.54	1.83
$\phi' = 20^\circ$	53.4	0.23	0.97	53.4	0.45	1.93	53.4	0.67	2.91
$\phi' = 30^\circ$	58.6	0.25	1.50	58.6	0.50	3.00	58.6	0.75	4.92
	α^{3D}	η^{3D}	N_γ^{3D}	α^{3D}	η^{3D}	N_γ^{3D}	α^{3D}	η^{3D}	N_γ^{3D}
$\phi' = 10^\circ$	47.0	0.32	1.02	47.0	0.62	2.03	47.0	0.93	3.05
$\phi' = 20^\circ$	48.9	0.41	2.46	49.0	0.84	4.91	48.9	1.00	7.48
$\phi' = 30^\circ$	49.4	0.50	7.22	49.4	0.94	14.45	49.4	1.00	22.57

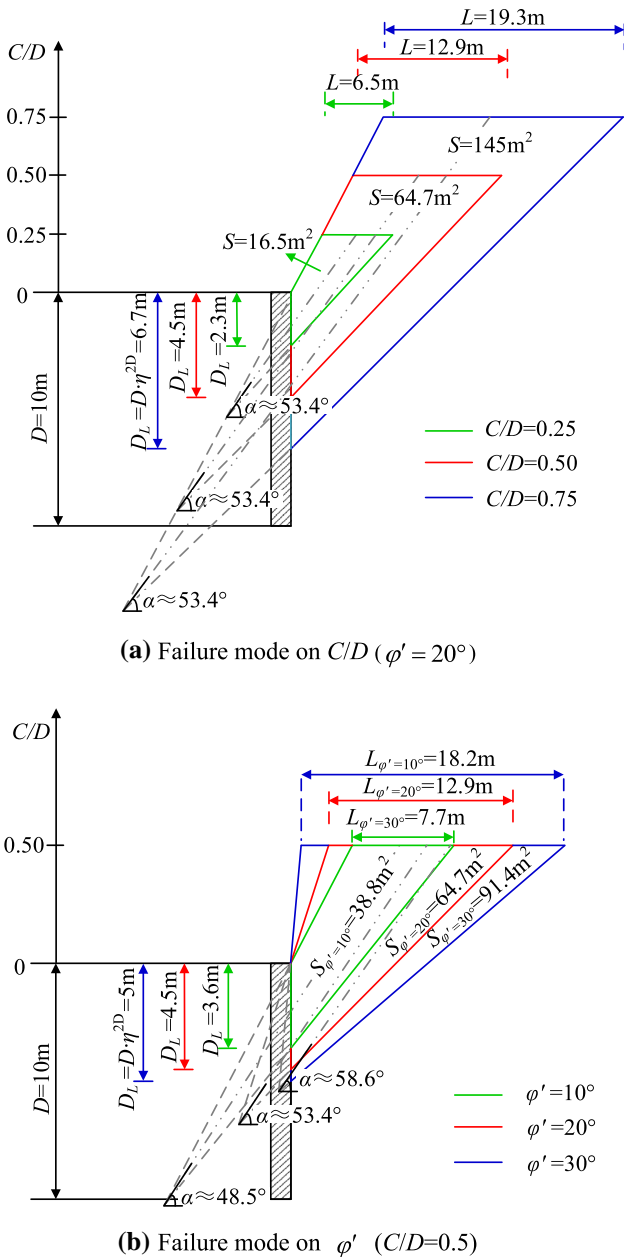


Fig. 4 Failure mode in mechanism MI. Failure mode on a C/D ($\phi' = 20^\circ$), b ϕ' ($C/D = 0.5$)

keeps at a constant of 0.5. The variation of failure pattern is more complicated because both the α^{2D} and the η^{2D} increase with the increase in ϕ' . As ϕ' increases from 10° to 30° , the area of the failure block increase by about 230% from 38.8 to 91.4 m^2 .

The three-dimensional mechanism MII shows a similar variation pattern with that of the two-dimensional mechanism MI. Figure 5a shows that with the increase in the C/D value while keeps a constant ϕ' , the inclination angle α^{3D} of the failure block keeps constant, while the depth ratio η^{3D} increases almost linearly. The volume of the failure

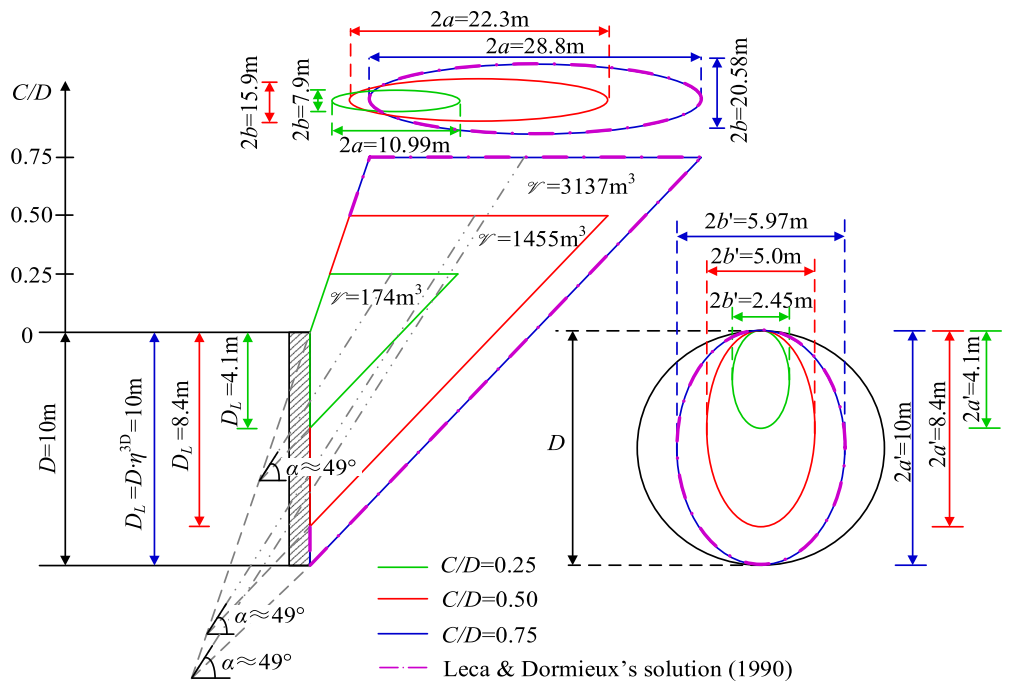
block increases, and the failure block expands at the ground surface. As C/D increases from 0.25 to 0.75, the volume of the failure block increases by about 1800% from 174 to 3137 m^3 . It is noted that when $\eta^{3D} = 1$ the failure mode in mechanism MII is identical to that derived by Leca and Dormieux [14]. This means that the general solution developed in this study converges to the particular 3D solution developed by Leca and Dormieux [14]. Figure 5b shows the variation of failure block when ϕ' varies, while C/D keeps at a constant, both the inclination angle α^{3D} and the depth ratio η^{3D} increase. As ϕ' increases from 10° to 30° , the volume of the failure block increases by nearly 950% from 437 to 4154 m^3 . The volume of failure block is sensitive to both ϕ' and C/D .

Figure 6 plots the variation of N_γ with the variation of the frictional angle ϕ' . Both N_γ^{2D} and N_γ^{3D} increase non-linearly with the increasing ϕ' . Compared with the N_γ^{2D} , N_γ^{3D} is much more sensitive to the ϕ' . In particular, when ϕ' is higher than 30° , the N_γ^{3D} value tends to diverge. The significant increase in N_γ^{3D} with the increase in ϕ' is consistent with the passive coefficient $K_{p\gamma}$ found by Soubra et al. [27].

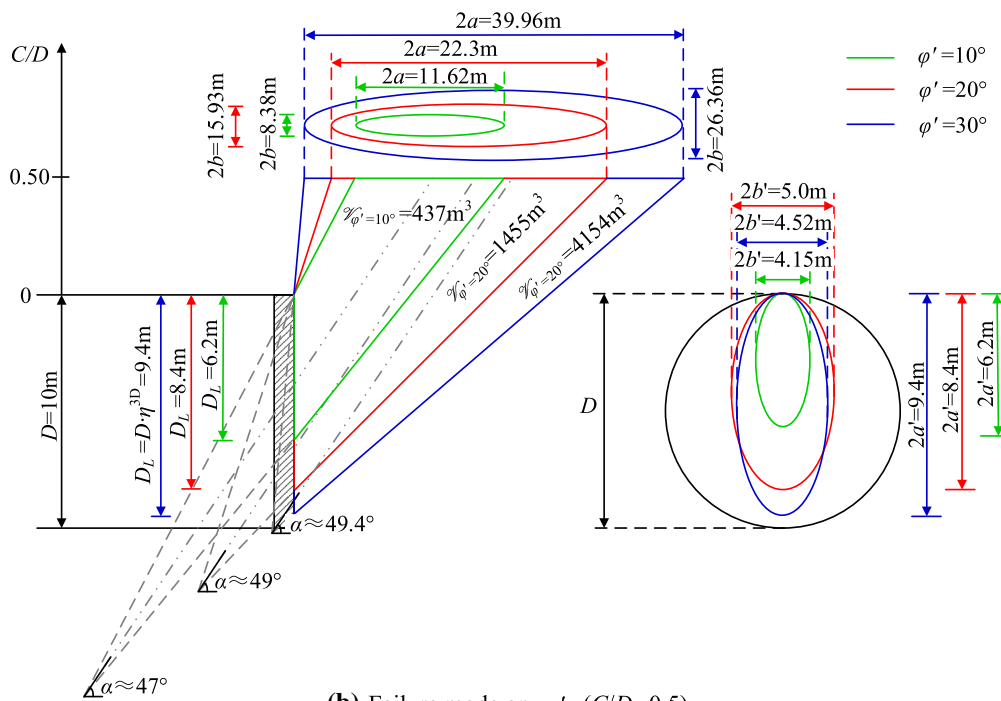
Figure 7 plots the variation of N_γ with the variation of the depth ratio C/D . Both N_γ^{2D} and N_γ^{3D} increase linearly with the increase in C/D . When ϕ' is relatively low (i.e., $\phi' = 10^\circ$), N_γ^{2D} and N_γ^{3D} are close to each other. However, when ϕ' is relatively high (i.e., $\phi' = 30^\circ$), N_γ^{3D} is significantly higher than N_γ^{2D} and the difference between N_γ^{2D} and N_γ^{3D} increase with the increasing ϕ' . It indicates that the sensitivity of N_γ^{3D} to C/D increases with increasing ϕ' .

When the soil has cohesion c' , Eqs. (4) and (8) contain the variables N_γ and N_s , which are the function of c' , ϕ' and η . To investigate the effect of cohesion c' on the support pressure, the tunnel, as shown in Fig. 1, is assumed to be buried in soils with both c' and ϕ' .

Figure 8 shows the effect of c' on N_γ for a tunnel with constant $C/D = 0.25$. It shows that with the same ϕ' , both N_γ^{2D} and N_γ^{3D} slightly increases with the increase in the c' . Compared to ϕ' , the impact of c' on N_γ^{2D} and N_γ^{3D} is much smaller. Figure 9 shows the effect of c' on N_s for a tunnel with constant $C/D = 0.25$. It shows that both N_s^{2D} and N_s^{3D} increase nonlinearly with the increasing ϕ' . Compared with the N_s^{2D} , N_s^{3D} is much more sensitive to the ϕ' . For the same ϕ' , both N_s^{2D} and N_s^{3D} slightly decrease with increasing c' . Similar to N_γ , the influence of c' on N_s^{2D} and N_s^{3D} is much smaller compared to that of the ϕ' . In general, the cohesion c' has a much smaller impact on the support pressure than that of the frictional angle ϕ' .



(a) Failure mode on C/D ($\phi' = 20^\circ$)



(b) Failure mode on ϕ' ($C/D=0.5$)

Fig. 5 Failure mode in mechanism MII

Figure 10 shows the effect of c' on N_γ for a tunnel with a varying C/D value. Figure 10a shows that at a relatively low frictional angle (i.e., $\phi' = 10^\circ$), N_γ^{2D} and N_γ^{3D} slightly increase with the increasing c' for a small C/D (i.e., $C/$

$D = 0.25$) and the effect of c' fades as C/D increases. Figure 10b shows that for a relatively higher frictional angle (i.e., $\phi' = 30^\circ$), with the increase in c' , N_γ^{2D} changes slightly while N_γ^{3D} keeps virtually constant. This indicates

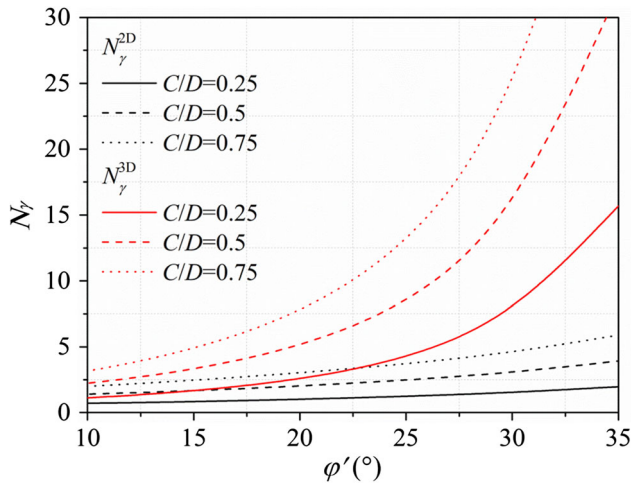


Fig. 6 Variation of N_γ^{3D} with ϕ' for cohesionless soil

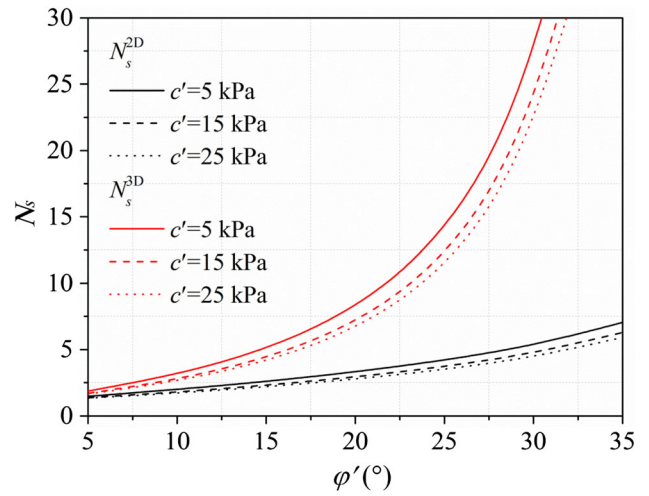


Fig. 9 Variation of N_s with c' and ϕ' ($C/D = 0.25$)

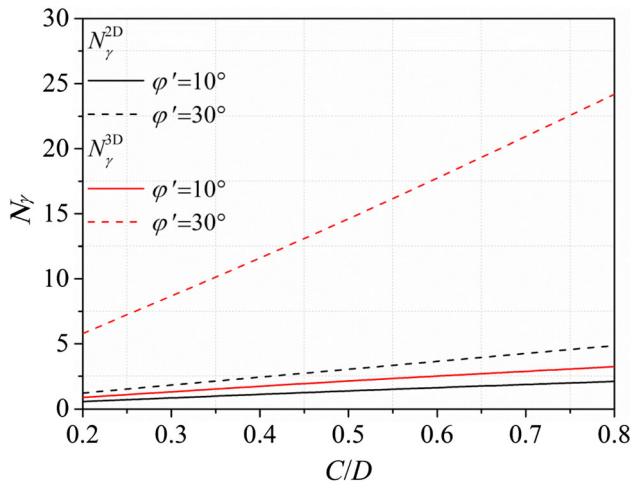
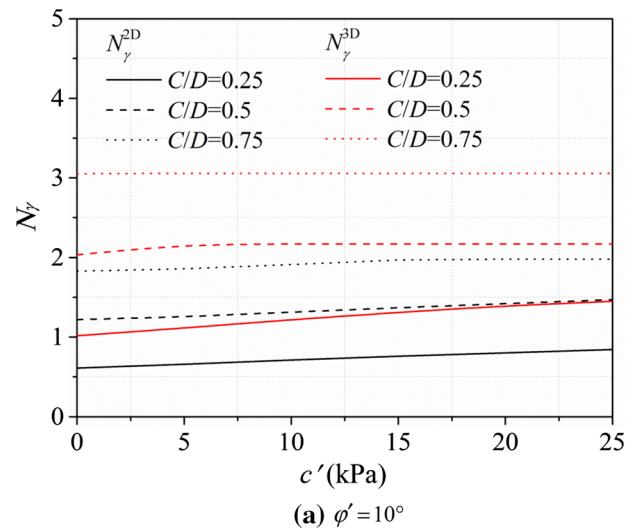


Fig. 7 Variation of N_γ with C/D for cohesionless soil



(a) $\phi' = 10^\circ$

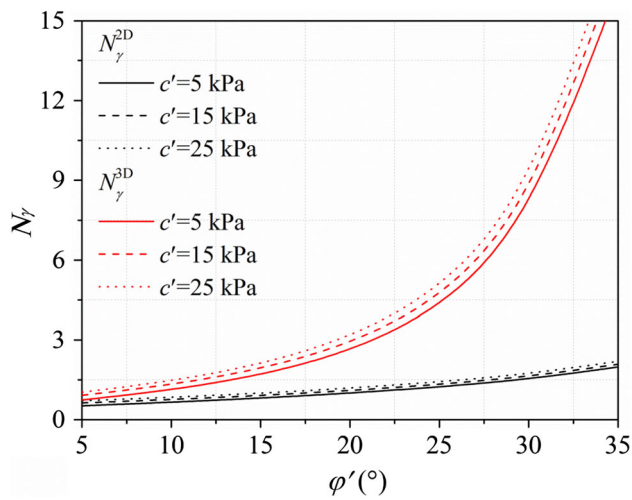
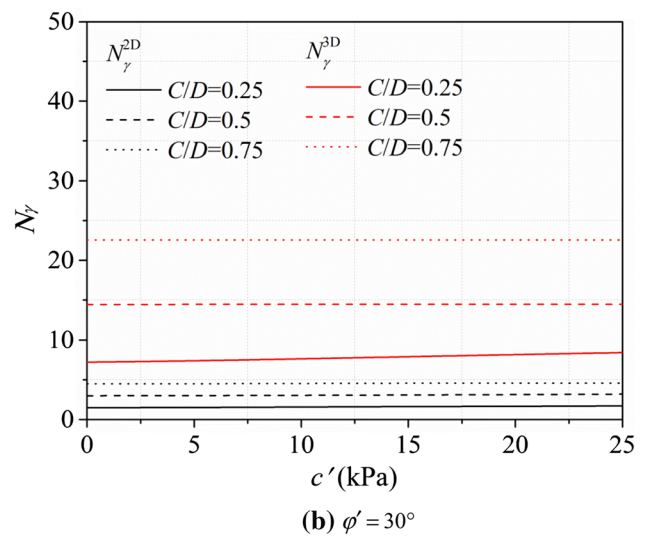


Fig. 8 Variation of N_γ with c' and ϕ' ($C/D = 0.25$)



(b) $\phi' = 30^\circ$

Fig. 10 Influence of c' on N_γ with different C/D values

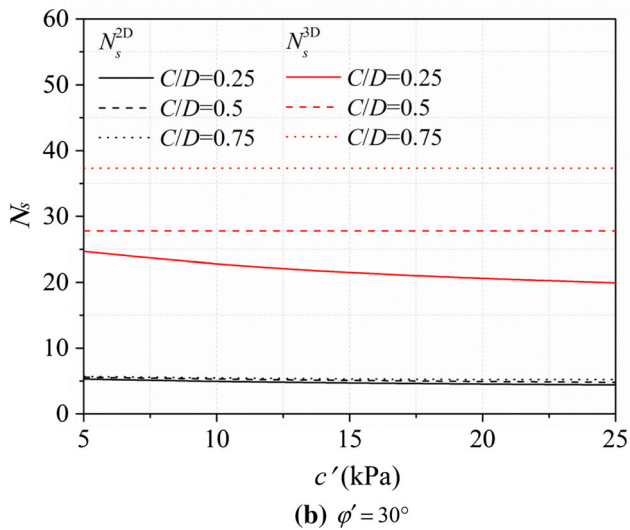
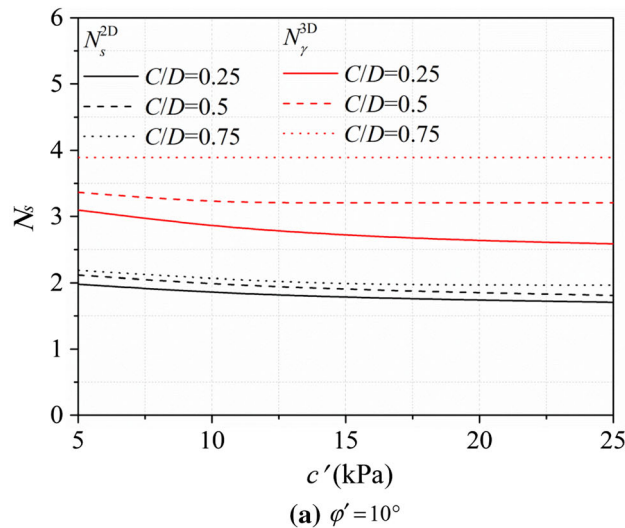


Fig. 11 Influence of c' on N_s with different C/D values

that the effect of c' on N_γ decreases with the increase in C/D value.

Figure 11 shows the effect of c' on N_s for a tunnel with varying C/D value. Figure 11a shows that at a low frictional angle (i.e., $\phi' = 10^\circ$), with the increase in c' , N_s^{2D} and N_s^{3D} decrease at a relatively low C/D value (i.e., $C/D = 0.25$) and the effect of c' on N_s fades at a relatively high C/D value (i.e., $C/D = 0.75$). Figure 11b shows that at a relatively higher frictional angle ($\phi' = 30^\circ$), with the increase in c' , N_s^{2D} slightly decreases while N_s^{3D} kept virtually constant except for the relatively lower $C/D = 0.25$. This indicates that the effect of c' on N_s decreases with the increase in C/D value.

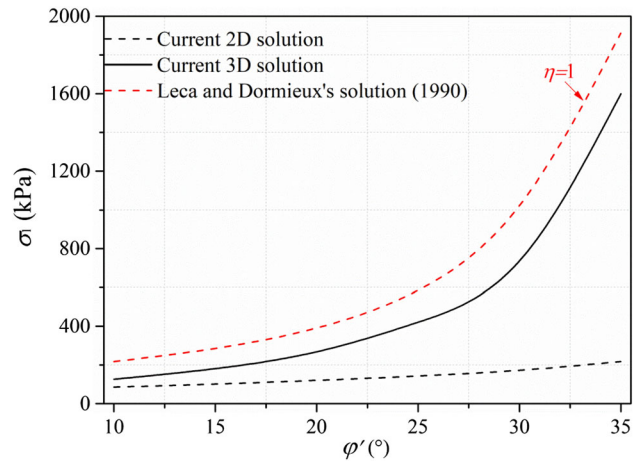


Fig. 12 Comparison on the support pressure for the case of $C/D = 0.25$

3.2 Support pressure

The current solutions on support pressure are compared with the Leca & Dormieux's solution [14] which is a 3D upper-bound solution with the assumption that the failure zone originates from the tunnel invert, i.e., $\eta = 1$. The cohesionless soils are used as an example. Figure 12 shows the comparison on the support pressure when $C/D = 0.25$. The support pressure from all the solutions nonlinearly increases with the increase in ϕ' . The support pressure from current 3D solution has similar variation trend as that from Leca and Dormieux's solution [14], but with constantly smaller values. This is because the Leca and Dormieux's solution [14] assumes the failure originates from the tunnel invert while the current solution predicts that the failure originates at a depth above tunnel invert when $C/D = 0.25$. The current 2D solution predicts much smaller support pressures than 3D solution due to the plain-strain assumption. For real three-dimensional problems, the

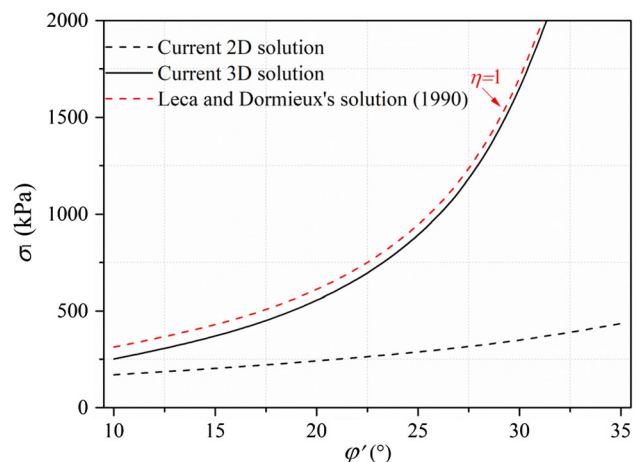


Fig. 13 Comparison of the support pressure for the case of $C/D = 0.5$

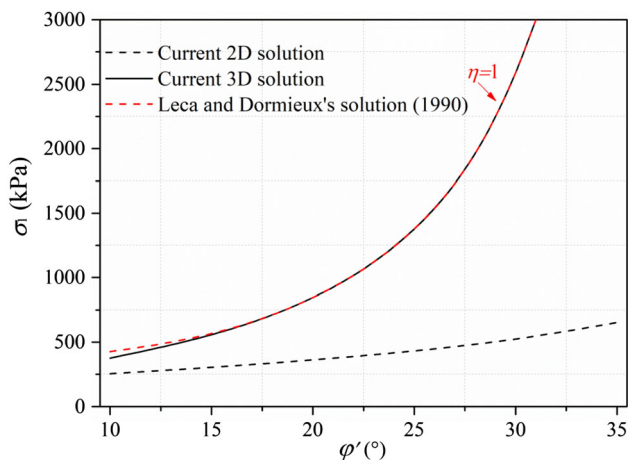


Fig. 14 Comparison of the support pressure for the case of $C/D = 0.75$

plain-strain mechanism typically overestimates the risk of failure [5, 19].

Figure 13 shows the comparison when $C/D = 0.5$. This figure shows that the current 3D solution is close to the Leca and Dormieux’s solution and the difference between these two solutions decreases with the increase in ϕ' . Referring to Table 1, as ϕ' increases from 10° to 35° , the η^{3D} varies from 0.80 to 0.94 approaching to 1, as assumed in the Leca and Dormieux’s solution [14]. The 2D solution predicts much lower support pressures than the 3D solutions.

Figure 14 shows the comparison on the support pressure when $C/D = 0.75$. Table 1 shows that the η^{3D} ranges from 0.93 to 1 as ϕ' increases from 10 to 35° when $C/D = 0.75$. As such, the current 3D solution converges to and Leca & Dormieux’s solution when $\phi' \geq 15^\circ$ at which $\eta^{3D} = 1$. The convergence of the current solution to Leca & Dormieux’s

Table 2 Soil properties

Layer	Soil type	w (%)	γ_{total} (kN/m ³)	c' (kPa)	ϕ' (°)	E (MPa)	K_0
①	Fill		18	3	16		
②	Sandy silt	27.9	18.8	6	25	9.0	0.40
③	Sandy silt and clay	40.5	17.5	15	10.7	2.8	0.56
④	Silty clay	30.7	18.9	37	16	5.5	0.37
⑤	clay	36.4	18.0	30	14	4.2	0.37

solution [14] verifies the current solution. The Leca & Dormieux’s solution [14] solution is a particular solution of the current 3D solution in which $\eta^{3D} = 1$.

4 Application of the analytical solutions

The derived 2D and 3D solutions were applied to a real project for validation. The Huanbei tunnels, located in Hangzhou, China, had a length of 1355 m and were driven by 11.6 m slurry shield. As shown in Fig. 15, the left tunnel was buried within stratum ② sandy silt and underlain with stratum ③ sandy silt and clay, stratum ④ silty clay and stratum ⑤ clay. The properties of the soil strata are summarized in Table 2.

As the SS shield launched from the shaft (SK5 + 800), the soil cover above tunnel crown is about 5 m. The alignment slightly inclined to keep a thicker soil cover above the tunnel crown. It is necessary to enhance the support pressure to resist against the increasing earth

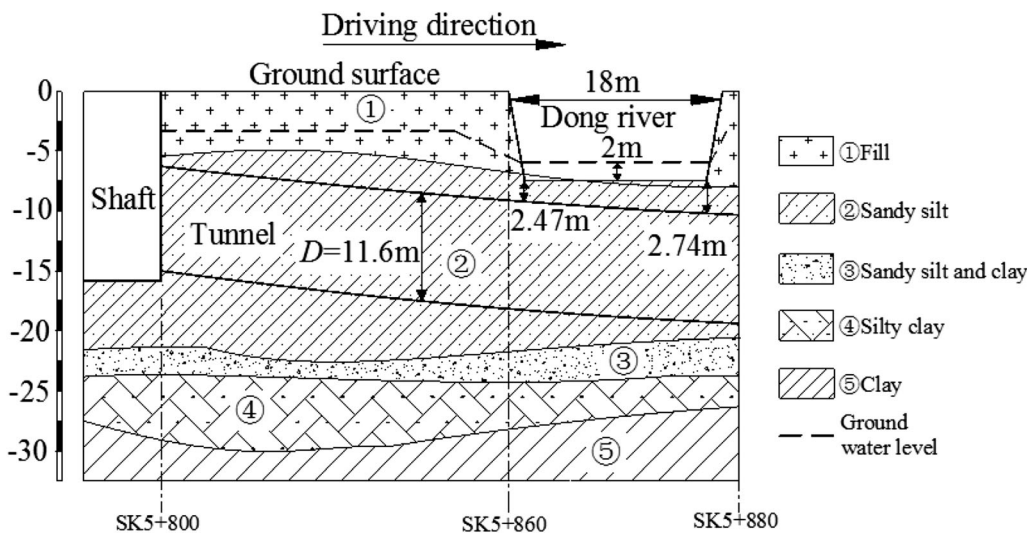


Fig. 15 The profile of geological conditions

Table 3 Results of the case in Huanbei tunnel

	Leca and Dormieux's solution [14]	This study	
		2D	3D
η	1	0.3	0.56
σ_1 (kPa)	680	252	625

pressure. As the SS shield approached to the bottom of Dong river (SK5 + 860), the thickness of the cover above the tunnel crown suddenly dropped to approximate 2.5 m. The width of the riverbed is about 18 m and the water level is 2 m above the riverbed. The sudden drop of cover depth substantially reduced the earth pressure at the working face. If the support pressure was not well controlled, it might generate face passive instability.

For the calculation, the tunnel diameter and the depth of soil cover above tunnel crown are idealized as 11.6 m and 2.5 m, respectively. The water level is 2 m above the riverbed. The calculation results are listed in Table 3. Leca and Dormieux's solution [14] predicts an ultimate support pressure of 680 kPa and the ratio $\eta = 1$ indicating that the face instability originated from the tunnel invert. The current 2D solution predicts an ultimate support pressure of 252 kPa and a depth ratio of $\eta = 0.3$ and the 3D solution predicts an ultimate pressure of 625 kPa and a depth ratio of $\eta = 0.56$. The Leca and Dormieux's solution [14] is about 10% higher than the current 3D solution. The current 3D solution predicted relatively smaller support pressure as well as the corresponding failure pattern. This solution indicates that the upper part of face potentially fails before the support pressure reaches the limit predicted by Leca and Dormieux's solution [14]. By taking a factor of safety of 2.0, the design slurry pressure was limited to 300 kPa to provide safety margin. The actual slurry pressure was measured ranging from 200 to 275 kPa during the tunneling process, and the working face stability was well controlled.

5 Conclusions

This paper develops the 2D and 3D kinematically admissible mechanisms for analyzing the passive face stability during slurry shield tunneling using the upper-bound analysis. The mechanisms consider trapezoidal distribution of slurry pressure along tunnel face and partial face failure. The mechanisms are verified by comparing the current solutions with the previous upper-bound solution. The mechanisms are validated through application to a practical

project of shallowly buried large diameter underwater tunnel.

For cohesionless soils, the support pressure is a function of soil effective frictional angle ϕ' which determines the inclination of failure block and the normalized soil cover depth C/D (soil cover depth/tunnel diameter) which, together with the effective frictional angle ϕ' , determines the origination of passive failure. The support pressure is sensitive to both ϕ' and C/D . The 3D solution is more sensitive to the effective frictional angle ϕ' and normalized soil cover depth C/D than the 2D solution. For cohesive soils, the support pressure is a function of ϕ' , C/D and effective cohesion c' . However, the effective cohesion c' has a relatively smaller impact on the support pressure.

The comparison between the current solution with previous upper-bound solution by Leca & Dormieux [14] shows that the current solution is a general solution to tunnel passive stability analysis. The Leca & Dormieux's solution is a particular solution of the current solution by assuming the face failure originating from the tunnel invert. The two solutions converge when the burial depth ratio η higher than 0.75. The application of the proposed mechanisms to the Huanbei Tunnel in China shows that the mechanisms are able to assess the tunnel face passive failure rationally.

Acknowledgements This research is supported by the National Natural Science Foundation of China (Grant Nos. 51508503 and 51778386), the Natural Science Foundation of Jiangsu Province (Grant No. BK20160320) and the Natural Science Fund of Colleges and Universities in Jiangsu Province (16KJB560012). The financial supports are gracefully acknowledged.

Appendix 1: Derivation of upper-bound solution for mechanism MI

As shown in Fig. 3, the triangles OAB and ODC have the same apex O and the same axis OM. The moving quadrilateral block ABCD corresponds to triangle ODC minus triangle OAB. The triangle ODC intersects the tunnel face AE along the line AB. The length of AB equals the height D_L of the partial failure area. Line DC represents the intersection between the ODC and the ground surface.

The power P_{σ_t} of support pressure on AB is

$$P_{\sigma_t} = \int_{AB} \bar{\sigma}_t \cdot \bar{V} ds = (\sigma_1 + \gamma_F \eta D/2) \eta DV \cos \alpha. \quad (14)$$

The power P_γ of soil weight within the block ABCD is

$$P_\gamma = \iint_{ABCD} \vec{\gamma}' \cdot \vec{V} ds = \gamma V \sin \alpha \iint_{ABCD} ds$$

$$= \gamma' V \sin \alpha \left[\frac{(C + \eta D)^2}{2 \tan(\alpha - \varphi')} - \frac{C^2}{2 \tan(\alpha + \varphi')} \right]. \tag{15}$$

The power P_{σ_s} of surcharge on DC is

$$P_{\sigma_s} = \int_{DC} \vec{\sigma}_s \cdot \vec{V} dl$$

$$= -\sigma_s V \sin \alpha \left[\frac{C + \eta D}{\tan(\alpha - \varphi')} - \frac{C}{\tan(\alpha + \varphi')} \right]. \tag{16}$$

The power P_e of external loads consists of the power P_{σ_t} of support pressure, the power P_γ of soil weight and the power P_{σ_s} of surcharge,

$$P_e = P_{\sigma_t} + P_\gamma + P_{\sigma_s}. \tag{17}$$

The power P_{vAD} of dissipation along the discontinues surface AD is

$$P_{vAD} = c' V \cos \varphi' \int_{AD} dl = \frac{c' V \cos \varphi'}{\sin(\alpha + \varphi')}. \tag{18}$$

The power P_{vBC} of the dissipation along the discontinuous surface

$$P_{vBC} = c' V \cos \varphi' \int_{BC} dl = \frac{c' V \cos \varphi' (C + \eta D)}{\sin(\alpha - \varphi')}. \tag{19}$$

The power of dissipation is

$$P_v = P_{vAD} + P_{vBC}. \tag{20}$$

By substituting Eqs. (14), (15) and (16) into Eq. (17) and substituting Eqs. (18) and (19) into Eq. (20), the upper-bound solution can be obtained in term of $P_e = P_v$. The 2D upper-bound solution of σ_1 can be rewritten in the compact form as

$$\sigma_1^{2D} = \gamma' D N_\gamma^{2D} + \sigma_s N_s^{2D} + c' N_c^{2D} - (\gamma_F - \gamma_w) \eta D / 2 + \gamma_w H, \tag{21}$$

where,

$$N_\gamma^{2D} = \frac{\tan \alpha}{2\eta} \left[\frac{(C/D + \eta)^2}{\tan(\alpha - \varphi')} - \frac{C^2/D^2}{\tan(\alpha + \varphi')} \right], \tag{22}$$

$$N_s^{2D} = \frac{\tan \alpha}{\eta} \left[\frac{C/D + \eta}{\tan(\alpha - \varphi')} - \frac{C/D}{\tan(\alpha + \varphi')} \right], \tag{23}$$

$$N_c^{2D} = \cot \varphi' (N_s^{2D} - 1). \tag{24}$$

Appendix 2: Derivation upper-bound solution for mechanism MII

As shown in Fig. 4, the conical block B corresponds to the cone C truncated by the cone C' . The intersection between cone C and the tunnel face is ellipse Σ' , while the intersection between cone C' and the ground surface is Σ . The coordinate system (O, x, y, z) is associated with the tunnel face and the origin is located at the center of Σ' . The other coordinates (Ω, X, Y, Z) are associated with the cones. The relationship between the two systems is linked by the following equations,

$$X = x, \tag{25}$$

$$Y = \frac{D_L}{2} \sin \alpha \tan \varphi' + y \cos \alpha - z \sin \alpha, \tag{26}$$

$$Z = \frac{D_L \cos \alpha}{2 \tan \varphi'} + y \cos \alpha + z \sin \alpha. \tag{27}$$

The height h of the cone C is

$$h = \frac{D_L}{2} \left(1 + \frac{\sin 2\alpha}{\sin 2\varphi'} \right) + C. \tag{28}$$

The height of the cone C' is

$$h' = \frac{D_L \cos(\alpha - \varphi') \cos(\alpha + \varphi')}{\sin 2\varphi'}. \tag{29}$$

The semi-axis a' and b' of the intersection Σ' are

$$a' = D_L / 2. \tag{30}$$

$$b' = \frac{D_L \sqrt{\cos(\alpha - \varphi') \cos(\alpha + \varphi')}}{2 \cos \varphi'}. \tag{31}$$

The area $S_{\Sigma'}$ of the intersection Σ' is

$$S_{\Sigma'} = \pi a' b' = \frac{\pi D_L^2 \sqrt{\cos(\alpha - \varphi') \cos(\alpha + \varphi')}}{4 \cos \varphi'}. \tag{32}$$

The semi-axis a and b of the intersection Σ are

$$a = \frac{C + D_L}{2 \tan(\alpha - \varphi')} - \frac{C}{2 \tan(\alpha + \varphi')}, \tag{33}$$

$$b = \frac{\sqrt{\sin(\alpha - \varphi') \sin(\alpha + \varphi')}}{2 \cos \varphi'} \left[\frac{C + D_L}{\tan(\alpha - \varphi')} - \frac{C}{\tan(\alpha + \varphi')} \right]. \tag{34}$$

The area S_Σ of the intersection Σ is

$$S_\Sigma = \pi ab = \frac{\pi \sqrt{\sin(\alpha - \varphi') \sin(\alpha + \varphi')}}{4 \cos \varphi'} \left[\frac{C + D_L}{\tan(\alpha - \varphi')} - \frac{C}{\tan(\alpha + \varphi')} \right]^2. \tag{35}$$

The volume V of cone C is

$$V = \frac{\pi}{12} \frac{\sqrt{\sin(\alpha - \varphi') \sin(\alpha + \varphi')}}{\cos \varphi'} \left[\frac{C + D_L}{\tan(\alpha - \varphi')} - \frac{C}{\tan(\alpha + \varphi')} \right]^2 \left[\frac{D_L}{2} \left(1 + \frac{\sin 2\alpha}{\sin 2\varphi'} \right) + C \right] \tag{36}$$

The area S of the lateral surface of cone C is

$$S = \frac{\pi \sin \alpha \sqrt{\sin(\alpha - \varphi') \sin(\alpha + \varphi')}}{4 \sin \varphi' \cos \varphi'} \left[\frac{C + D_L}{\tan(\alpha - \varphi')} - \frac{C}{\tan(\alpha + \varphi')} \right]^2 \tag{37}$$

The volume V' and the lateral surface area S' of cone C' are

$$V' = \frac{\pi d^3 [\cos(\alpha - \varphi') \cos(\alpha + \varphi')]^{\frac{3}{2}}}{12 \cos \varphi' \sin 2\varphi'} \tag{38}$$

$$S' = \frac{\pi d^2 \cos \alpha \sqrt{\cos(\alpha - \varphi') \cos(\alpha + \varphi')}}{4 \sin \varphi' \cos \varphi'} \tag{39}$$

The volume V_b and the lateral surface area S_b of block B are obtained, respectively, by

$$V_b = V - V' \tag{40}$$

$$S_b = S - S' \tag{41}$$

By introducing the coefficients

$$R_A = \sqrt{\tan(\alpha - \varphi') \tan(\alpha + \varphi')} \left[\frac{\eta + C/D}{\tan(\alpha - \varphi')} - \frac{C/D}{\tan(\alpha + \varphi')} \right]^2 \tag{42}$$

$$R_B = \frac{\eta}{2} \left(1 + \frac{\sin 2\alpha}{\sin 2\varphi'} \right) + \frac{C}{D} \tag{43}$$

$$R_C = \frac{\eta \cos(\alpha - \varphi') \cos(\alpha + \varphi')}{\sin 2\varphi'} \tag{44}$$

The volume V_b and lateral surface area S_b can be simplified as

$$V_b = \frac{\pi D^3 \sqrt{\cos(\alpha - \varphi') \cos(\alpha + \varphi')}}{12 \cos \varphi'} [R_A R_B - \eta^2 R_C] \tag{45}$$

$$S_b = \frac{\pi D^2 \sqrt{\cos(\alpha - \varphi') \cos(\alpha + \varphi')}}{4 \sin \varphi' \cos \varphi'} [\sin \alpha R_A - \eta^2 \cos \alpha] \tag{46}$$

The power P_e of external loads applying on the mechanism consists of the power P_{σ_t} of the support pressure, the power P_{σ_s} of surcharge and power P_γ of the soil weight,

$$P_e = P_{\sigma_t} + P_{\sigma_s} + P_\gamma \tag{47}$$

The power P_{σ_t} of support pressure is

$$P_{\sigma_t} = \sigma_t \frac{\pi V \eta^2 D^2 \cos \alpha \sqrt{\cos(\alpha - \varphi') \cos(\alpha + \varphi')}}{4 \cos \varphi'} \tag{48}$$

The power P_{σ_s} of surcharge on the ground surface is

$$P_{\sigma_s} = -\sigma_s \frac{\pi V D^2 \sin \alpha \sqrt{\cos(\alpha - \varphi') \cos(\alpha + \varphi')}}{4 \cos \varphi'} R_A \tag{49}$$

The power P_γ of soil weight is

$$P_\gamma = -\gamma' \frac{\pi V D^3 \sin \alpha \sqrt{\cos(\alpha - \varphi') \cos(\alpha + \varphi')}}{4 \cos \varphi'} [R_A R_B - \eta^2 R_C] \tag{50}$$

Substituting Eqs. (48), (49) and (50) into Eq. (47), P_e is rewritten as

$$P_e = \frac{\pi V D^2 \sin \alpha \sqrt{\cos(\alpha - \varphi') \cos(\alpha + \varphi')}}{4 \cos \varphi'} \left[\sigma_t \cot \alpha - \sigma_s R_A - \frac{\gamma' D}{3} (R_A R_B - R_C) \right] \tag{51}$$

The mechanism block is rigid so that the dissipation of the plastic energy occurs along the discontinuous surface. With the associated flow, the dissipation energy per area $dP_v/d\Sigma$ is

$$\frac{dP_v}{d\Sigma} = c' V \cos \varphi' \tag{52}$$

The dissipation power P_v along the lateral surface of the mechanism block B is

$$P_v = \iint_B \frac{dP_v}{d\Sigma} = c' V \cos \varphi' S_b \tag{53}$$

where S_b is the area of lateral surface of the block B .

Substituting equation (46) for S_b , Eq.(53) can be written as

$$P_v = c' \frac{\pi V D^2 \sqrt{\cos(\alpha - \varphi') \cos(\alpha + \varphi')}}{4 \sin \varphi'} [R_A \sin \alpha - \eta^2 \cos \alpha] \tag{54}$$

By introducing Eqs. (51) and (54) into the equation $P_e = P_v$, the upper-bound solution can be obtained. Subsequently, the 3D upper-bound solution of can be rearranged as

$$\sigma_1^{3D} = \gamma' D N_\gamma^{3D} + \sigma_s N_s^{3D} + c' N_c^{3D} - (\gamma_F - \gamma_w) \eta D / 2 + \gamma_w H \tag{55}$$

where,

$$N_s^{3D} = \frac{\tan \alpha R_A}{\eta^2} \tag{56}$$

$$N_\gamma^{3D} = \frac{\tan \alpha}{3\eta^2} (R_A R_B - \eta^2 R_C) \tag{57}$$

$$N_c^{3D} = \cot \varphi' (N_s^{3D} - 1) \tag{58}$$

References

- Anagnostou G, Kovári K (1994) The face stability of slurry shield-driven tunnels. *Tunn Undergr Space Technol* 9(2):165–174
- Anagnostou G, Kovári K (1996) Face stability conditions with earth pressure balanced shields. *Tunn Undergr Space Technol* 11(2):165–173
- Bezuijen A, Brassinga HE (2006) Blow-out pressure measured in a centrifuge model and in the field. *Tunnelling: a decade of progress: GeoDelft 1995–2005*. Taylor & Francis, USA
- Broere W (2001) Tunnel face stability & new CPT applications. Ph.D. Thesis, Delft University Press
- Chen WF (1975) *Limit analysis and soil plasticity*. Elsevier, Amsterdam
- Chen RP, Li J, Kong LG, Tang LJ (2013) Experimental study on face instability of shield tunnel in sand. *Tunn Undergr Space Technol* 33(1):12–21
- Clough GW, Sweeney SP, Finno RJ (1983) Measured soil response to EPB shield tunnelling. *J Geotech Eng Div Am Soc Civ Eng* 109(2):131–149
- Davis EH, Gunn MJ, Mair RJ, Seneviratne HN (1980) The stability of shallow tunnels and underground opening in cohesive material. *Géotechnique* 30(4):397–416
- Dias D, Janin JP, Sourba AH, et al (2008) Three-dimensional face stability analysis of circular tunnels by numerical simulation. In: *Proceeding of geo-congress: characterization, monitoring, and modeling of geo-system*. Louisiana: ASCE, pp 886–893
- Gao YF, Zhang F, Lei GH, Li DY (2013) An extended limit analysis of three-dimensional slope stability. *Géotechnique* 63(6):518–524
- Gugliemetti V, Grasso P, Mahtab A, Xu SL (2008) *Mechanized tunnelling in urban areas*. Taylor & Francis Group, London
- Idinger G, Aklik P, Wu W, Borja RI (2011) Centrifuge model test on the face stability of shallow tunnel. *Acta Geotech* 6(4):105–117
- Kirsch A (2010) Experimental investigation of the face stability of shallow tunnels in sand. *Acta Geotech* 5(1):43–62
- Leca E, Dormieux L (1990) Upper bound and lower bound solutions for the face stability of shallow circular tunnels in frictional material. *Géotechnique* 40(4):581–606
- Li Y, Emeriault F, Kanstner R, Zhang ZX (2009) Stability analysis of slurry shield-driven tunnel in soft clay. *Tunn Undergr Space Technol* 24:472–481
- Liu W, Zhao Y, Shi P et al (2018) Face stability analysis of shield driven tunnels shallowly buried in dry sand using 1 g large-scale model tests. *Acta Geotech* 13(3):693–705
- Maidl B, Herrenknecht M, Maidl U et al (2012) *Mechanised shield tunnelling*, 2nd edn. Wilhelm Ernst & Sohn, Berlin
- Mair R (1979) *Centrifuge model testing of tunnel construction in soft ground*. Ph.D. Thesis, Cambridge University Press
- Michalowski RL, Drescher A (2009) Three dimensional stability of slopes and excavations. *Géotechnique* 59(10):839–850
- Mollon G, Dias D, Soubra AH (2011) Rotational failure mechanisms for the face stability analysis of tunnels driven by a pressurized shield. *Int J Numer Anal Meth Geomech* 35(12):1363–1388
- Mollon G, Dias D, Soubra AH (2013) Continuous velocity fields for collapse and blow-out of a pressurized tunnel face in purely cohesive soil. *Int J Numer Anal Meth Geomech* 37(13):2061–2083
- Ng CWW, Wong KS (2013) Investigation of passive failure and deformation mechanisms due to tunnelling in clay. *Can Geotech J* 50:359–372
- Oberlé S (1996) Face stability analysis of a circular tunnel by kinematical approach. Final Study Project, INSA, Strasbourg
- Shi P, Li P (2015) Mechanism of soft ground tunnel defect generation and functional degradation. *Tunn Undergr Space Technol* 50:334–344
- Soubra AH (2000) Three-dimensional face stability analysis of shallow circular tunnels. In: *Proceedings of the international conference on geotechnical and geological engineering*, Melbourne, Australia, pp 19–24
- Soubra AH (2002) Kinematical approach to the face stability analysis of shallow circular tunnels. In: *8th international symposium on plasticity*, Canada, British Columbia, pp 443–445
- Soubra AH, Regenass P (2000) Three-dimensional passive earth pressures by kinematical approach. *J Geotech Geo-environ Eng* 126(11):969–978
- Tang XW, Liu W, Albers B, Savidis S (2014) Upper bound analysis of tunnel face stability in layered soils. *Acta Geotech* 9(4):661–671
- Wong KS, Ng CWW, Chen YM, Bian XC (2012) Centrifuge and numerical investigation of passive failure tunnel face in sand. *Tunn Undergr Space Technol* 28(3):297–303
- WSSC (2015) *Tunnel design criteria in pipeline design manual*. Washington Suburban Sanitary Commission, Washington
- Zhang F, Gao YF, Wu YX, Zhang N (2018) Upper bound solutions for face stability of circular tunnels in undrained clays. *Géotechnique* 68(1):76–85
- Zhu WB, Ju SJ (2009) *Analysis of the risk resources and typical cases in shield tunnelling*. Jinan University Press (in Chinese)

Publisher's Note Springer Nature remains neutral with regard to jurisdictional claims in published maps and institutional affiliations.